Relation between Mean Boundary-Layer Structure and Cloudiness at the R/V *Valdivia* during ASTEX

ALAN K. BETTS

Atmospheric Research, Pittsford, Vermont

CHRISTOPHER S. BRETHERTON

Atmospheric Science Department, University of Washington, Seattle, Washington

ERNST KLINKER

European Centre for Medium-Range Weather Forecasts, Reading, England

(Manuscript received 8 July 1994, in final form 12 December 1994)

ABSTRACT

The relationship between boundary-layer thermodynamic structure and cloud fields and their diurnal variation are explored using seven days of data from the R/V *Valdivia* during the Atlantic Stratocumulus Transition Experiment. Cloudiness is at a maximum before dawn, when the boundary layer (BL) has the thermodynamic structure of a partially mixed, conditionally unstable stratocumulus layer, which is close to mean saturation below the inversion. Cloudiness falls during the daytime, and in the late afternoon the BL has two distinct layers: a warmer, drier cloud layer (characteristic of trade cumulus) above a more well-mixed subcloud layer. The observed mean profiles are consistent with an earlier suggestion that there is a cloud-cover transition once the BL mixing-line slope exceeds half that of the moist adiabat. In contrast, the BL structure in the ECMWF model for the same week has a much drier, warmer, more stable "cloud" layer than the observations.

1. Introduction

The prediction of boundary-layer (BL) clouds over the ocean in models remains a difficult parametric problem. Forecast and climate models use very simple parameterizations for clouds and their optical properties, usually based on thermodynamic properties averaged over a grid cell. In a companion paper, Bretherton et al. (1995) present an overview of the comparison between observations of BL cloudiness and structure and the cloud predicted diagnostically by the operational European Centre for Medium-Range Weather Forecasts (ECMWF) model during the Atlantic Stratocumulus Transition Experiment (ASTEX). They found that although the ECMWF model had a somewhat realistic representation of the BL structure and inversion, the diagnostic cloud algorithm underestimated mean cloudiness and had no measurable skill in predicting cloud variations, either diurnally or from day to day. This short paper examines the BL thermodynamic and cloud structure over the open ocean at the R/V *Valdivia* during ASTEX. Our intent is to relate BL structure to cloud cover to provide test datasets for the development of improved models for both cloud cover and the diurnal variation of the BL over the ocean. This was one key objective of ASTEX (Albrecht et al. 1995a). The R/V *Valdivia* was stationed at 28°N,24°W for the period 1–15 June 1992. The ship collected ceilometer data for the period 6–15 June. We analyze here the 7 days 8–14 June, during which the inversion height remained very steady near 850 mb, and radiosondes were launched every 3 h.

Corresponding author address: Alan K. Betts, RR3, Box 3125, Pittsford, VT 05763.

2. Observed BL profiles at the *Valdivia*

a. Diurnal variation

Figure 1 shows the diurnal cycle of hourly mean cloudiness for 8–14 June at the *Valdivia*, as measured by a lidar ceilometer. The ceilometer sampled every 30 s and could detect cloud bases up to 3.5 km (see Bretherton et al. 1995). The standard deviation is significant (about 25%), but most days show extensive BL cloud before and near sunrise and a minimum of BL cloudiness around local noon. The mean nighttime cloud-base height as measured by the lidar ceilometer is near 1100 m, which corresponds to 900 mb. This is close to the mean inversion base, suggesting that the layer clouds were typically thin. The diurnal variation of cloudiness

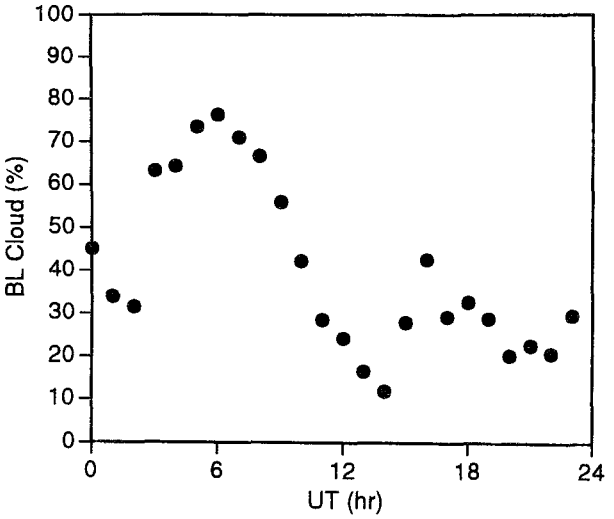

FIG. 1. Diurnal variation of mean cloudiness at R/V *Valdevia* for 8–14 June.

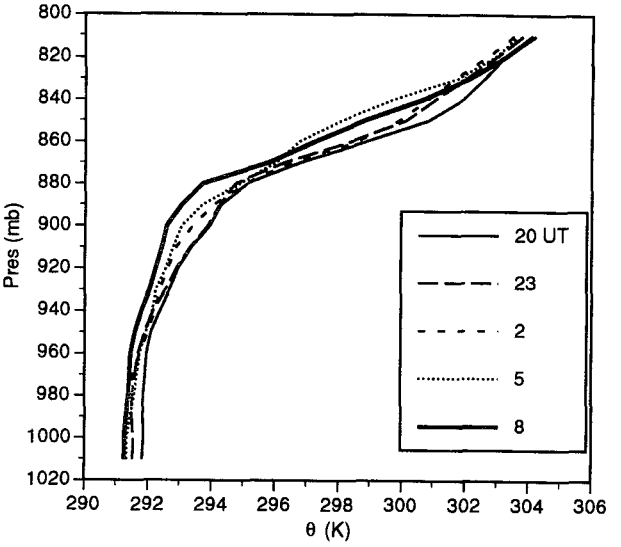

FIG. 2a. Profiles of time sequence of nighttime potential temperature θ, through boundary layer from 0200–0800 UTC (approx 1930–0630 local solar time).

at the *Valdivia* was larger than at the two ASTEX island sites of Santa Maria, in the Azores, and Porto Santo, in the Madeira Islands (Bretherton et al. 1995). However our 7-day analysis period is short and may not be representative. The data suggest links between the local diurnal variation of thermodynamic structure and the radiation field. However, it is also possible that there may also be diurnal variations in the horizontal advection of temperature and moisture, which are not resolved here.

Because the height of the inversion is quite steady near 850 mb, and sondes were launched on a regular schedule every 3 h (with none missing), a simple average of the 7 days shows the diurnal cycle of the BL. The nominal synoptic times are 0000, 0300, 0600, 0900 UTC, etc. (all times are UTC hereafter), but balloons were launched in ASTEX about 70 min prior to these nominal times (rather than a conventional 45 min) to allow extra time for data processing and transmission to the Global Telecommunications System.

Figure 2a shows a plot of potential temperature θ against pressure for the sequence of five nighttime averages. The times of these mean soundings through the BL are approximately 2000, 2300, 0200, 0500, and 0800 (corresponding to local solar times approximately 90 min earlier). All the mean profiles show a change of slope near 960 mb, the lifting condensation level of air near the surface, separating a nearly well-mixed subcloud layer from a more stable "cloud" layer above. The 2000 and 2300 averages are also the most stable in the cloud layer, probably as a result of daytime solar absorption (seen also in Betts 1990). The 2000 average near sunset is the warmest, and a clear, cooling trend can be seen during the night. The subcloud layer appears to cool first, followed by a cooling and destabilization of the cloud layer, presumably because of the coupling between the cloud field and the longwave radiative cooling. The 0800 average near sunrise is the coolest, as well as the most unstable in the cloud layer. Cloudiness reaches a maximum near 80% during the presunrise time period 0500–0800 (Fig. 1). There is a suggestion from Fig. 2a that the BL is deepest in this time period. Figure 2b shows the warming sequence during the daytime from 0800 to 2000. The 1100 mean is much warmer than the 0800 mean. It is probable that some of this increase is due to direct solar heating of the sonde thermistor, since cloudiness is also approaching a minimum near 1100. (The humidity data show

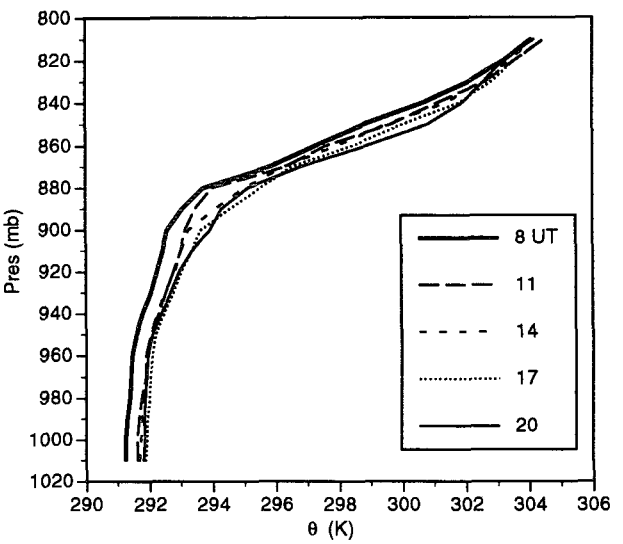

FIG. 2b. As in Fig. 2a for daytime profiles from 0800 to 2000 UTC.

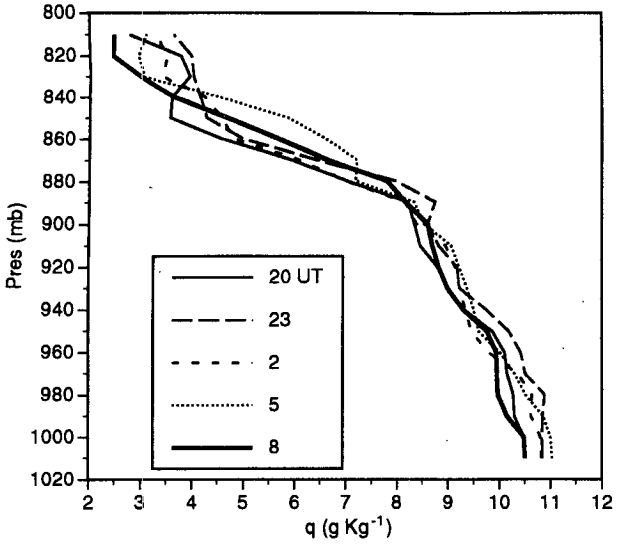

FIG. 3a. As in Fig. 2a for mixing ratio q.

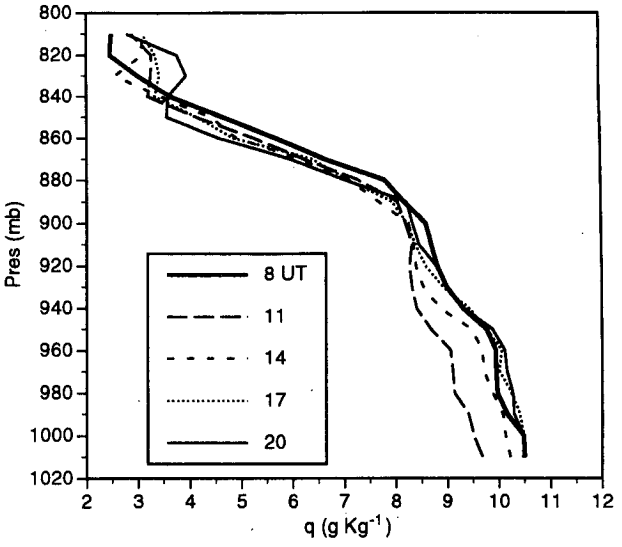

FIG. 3b. As in Fig. 2b for mixing ratio q.

signs of a larger error produced by solar heating. See below for more details.) By 1700, the BL has reached a maximum temperature; a very small cooling can be seen near cloud base between 1700 and 2000.

Figure 3a shows the corresponding mean moisture profiles for the nighttime hours from 2000 to 0800. The three that showed a cooling trend in the subcloud layer in Fig. 2a; namely, 2300, 0200, and 0500, are significantly moister, suggesting that destabilization near the surface might have increased the surface latent heat flux. The mean vertical motion profile from the ECMWF analyses (which has a large uncertainty) also suggests that subsidence is weak in this time period (see Fig. 13 later). By 0800, the subcloud layer has dried significantly, suggesting that this might be linked to the sharp fall of cloud cover shown in Fig. 1. Figure 3b continues the sonde sequence from 0800 to 2000 for the daytime period. The 1100 mean profile is drier by about 1 g kg^{-1} in the subcloud layer. We suspect this is not a true diurnal variation but results at least in part from solar heating of the humicap sensor on the *Vaisala* RS-80 sonde. Cloud cover is a minimum at this time. Similar problems with this instrument have been noted in the Tropical Oceans and Global Atmosphere Coupled Ocean–Atmosphere Response Experiment in the Western Pacific (Cole 1993). Unfortunately, this systematic humidity error due to solar radiation has not been studied, so the humidity data at 1100 and (probably) 1400 are suspect. We thus exclude these sonde times from our subsequent analyses.

From a modeling viewpoint this is unfortunate, because it means we do not have measurements of the whole BL diurnal variation, uncontaminated by daytime solar heating of the sonde sensors. However, the day–night differences are large and appear well represented by late afternoon and evening profiles and the predawn profiles, so they should provide useful reference profiles for modeling studies.

b. *Morning–evening BL profiles*

The sharpest contrast in BL structure with a strong correlation to cloudiness can be found by comparing averages of the predawn sondes at 0500 and 0800 with the average of the late afternoon sondes at 1700 and 2000. These morning and evening means are tabulated in the Appendix (see Table A.1). Figure 4 shows the profiles of θ and q. The evening structure, which cor-

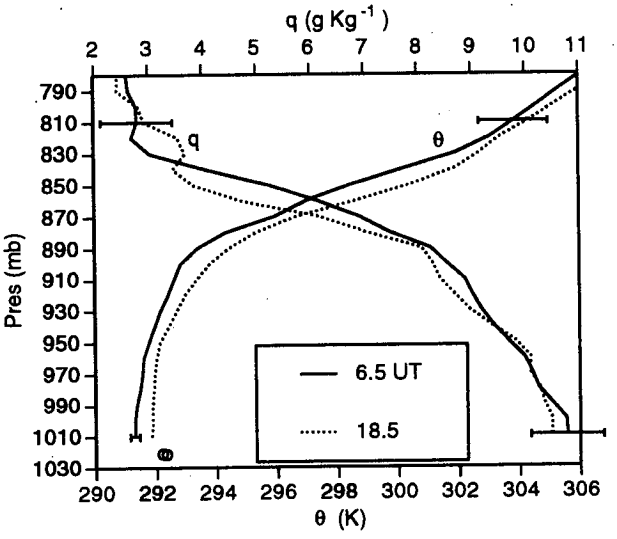

FIG. 4. Profiles of θ and q for morning and evening averages at 0630 and 1830 UTC.

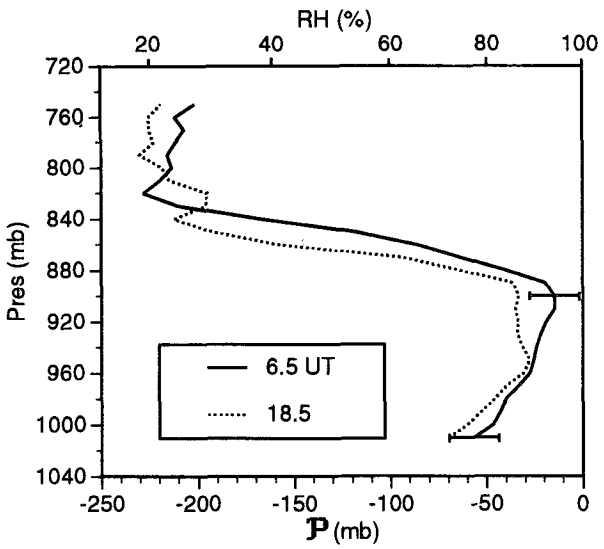

FIG. 5. Profiles of saturation pressure deficit: $P = p^* - p$ (upper scale is % relative humidity).

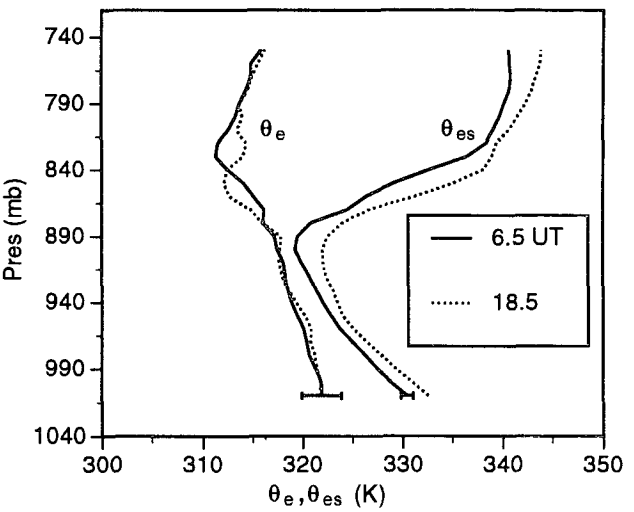

FIG. 6. As in Fig. 4 for θ_{es} and θ_e.

responds to a low BL cloud cover (about 28%), is more well mixed in θ and q in the subcloud layer (960–1010 mb) and less well mixed above (i.e., the gradients of θ and q with height are greater). In contrast, the predawn structure, when stratocumulus cover is high (about 72%), has a more stable θ structure for $p > 950$ mb and a more unstable structure in the cloud layer below the inversion ($950 > p > 900$ mb). The mixing ratio is higher near the surface and falls more uniformly with height. The sea surface temperature (SST) has a much smaller diurnal range from 20.82°C at 0630 to 20.99°C at 1830, with corresponding surface pressures and saturation mixing ratios of 1021.3 and 15.34 and 1021.5 mb and 15.50 g kg^{-1}, respectively. Figure 4 shows the corresponding SST θ values as open circles.

Because of the large atmospheric variability, it is never easy to assess the significance of the differences seen in atmospheric composites. For each day, we calculated the mean difference between the pairs of morning and evening sondes. The error bars on Fig. 4 are the standard deviations of this (evening–morning) difference for the 7 days, shown at two levels. In the subcloud layer, the standard deviation of the θ difference is considerably less than the difference between the means, but this is not true for pressures below 900 m (i.e., through and above the inversion). In moisture, however, the variability between days is much larger, and the standard deviation is larger than the mean difference at all levels. The changes in the vertical profiles appear, however, to be physically meaningful, but we do not have an objective test for this.

Figure 5 shows the derived profile of $P = p^* - p$, where p^* is the saturation pressure (Betts 1982); P is a measure of the pressure difference of a layer from saturation [related to the relative humidity (RH) in the BL, shown on the upper scale]. This shows again the more distinct two-layer structure of the late afternoon profile, as well as the more uniform predawn profile. We see that the predawn mean is closer to saturation, especially just below the inversion (where mean RH exceeds 93%). The difference between the means exceeds the standard deviation (calculated as in Fig. 4) at this level.

The final pairs of curves, shown in Fig. 6, are equivalent potential temperature θ_e and the saturation equivalent potential temperature θ_{es}. These show that the layer is closer to saturation as a result of the fall of θ_{es} (a function only of temperature and pressure), while the BL equilibrium of θ_e changes very little (much less than the standard deviation between different days). The predawn mean has marked BL conditional instability in the cloud layer, while the late afternoon BL does not. Figure 6 also shows the minimum of θ_e at inversion top, which has been seen in earlier studies of trade wind convection (Betts and Albrecht 1987; Kloessel and Albrecht 1989). In contrast, the First ISCCP Regional Experiment's San Nichols Island, California, stratocumulus soundings (Albrecht et al. 1995b) show that a very weak θ_e minimum is barely visible in the mean even after careful averaging.

TABLE 1. Partition by cloud cover at sonde launch times.

	Low cloud cover	High cloud cover
Cover	<25%	>25%
Number of cases	22	20
Mean cloud cover	10 ± 9%	80 ± 16%
Mean SST	20.91°C	20.85°C
Mean surface pressure	1022.3 mb	1021.3 mb

c. Partition by cloud cover

We also partitioned the sonde data using the ceilometer cloud cover (averaged for the hour centered on 0200, 0500, etc.) into two groups: above and below 25% cloud cover (Table 1). To reduce solar radiation errors, we again excluded the 1100 and 1400 sondes. The cloud distribution is highly nonuniform: The low cloud-cover group has a mean cover (and standard deviation) of 10 ± 9%, while the high cloud-cover group has a mean cover of 80 ± 16%, reflecting the bimodality of the cloud cover data. (The mean cloud cover is between 25% and 50% at only 8% of the hours at the Valdivia.) This partition suggests a direct link between cloudiness and BL structure. Figure 7 shows the profiles of $P = p^* - p$. There is a strong similarity to Fig. 5, although, not unexpectedly, the separation of the pair of curves is a little greater. The high cloud-cover average is closer to saturation near the inversion base (≈96%), while the low cloud-cover average is a little less saturated. Some standard deviations about the mean for each group are shown. Figure 8 shows the θ_e and θ_{es} profiles. In this partition of the data (which is distributed differently in time from Fig. 6), the mean values of subcloud temperature and moisture are similar (the differences are much less than the standard deviations of each group), although again the low cloud-amount average is more well mixed. The saturation level of air lifted from 1010 mb is 950 mb and in the cloud layer ($890 < p < 950$), the greater instability and higher humidity of the high cloud-cover average is apparent. These mean soundings are tabulated in the appendix (Table A.2).

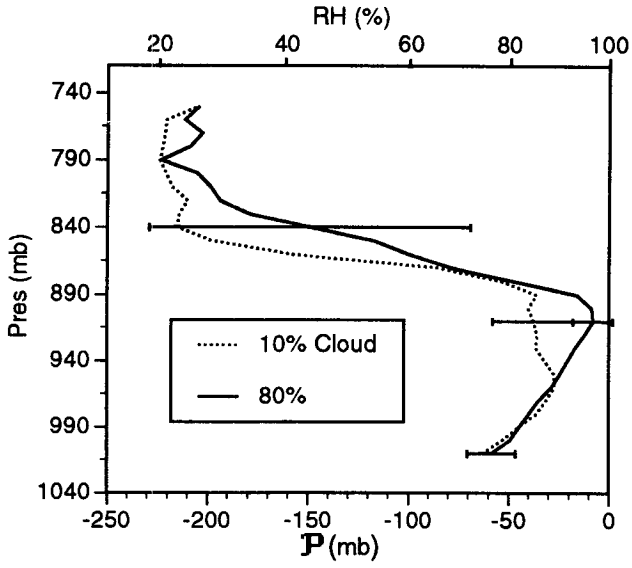

FIG. 7. As in Fig. 5 for high and low cloud-cover partition of sondes.

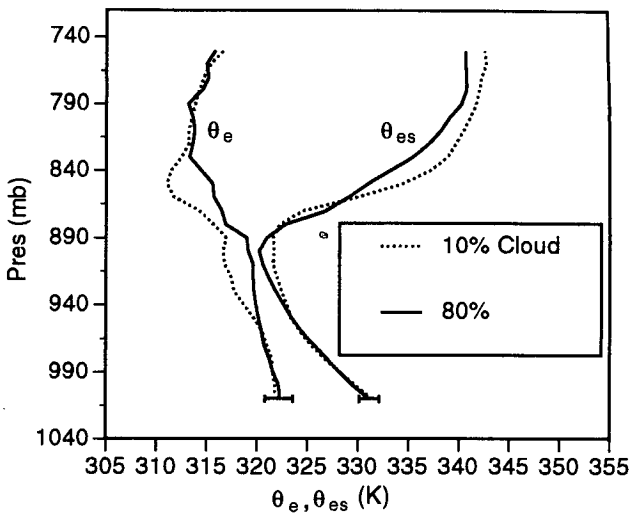

FIG. 8. As in Fig. 6 for high and low cloud cover partition of sondes.

3. Modeling conclusions

Bretherton et al. (1995) discuss several models that have been proposed for determining BL cloud cover, but they find only the observational link to RH. Figures 5 and 7 also show, not surprisingly, that cloud cover and relative humidity near the BL top are correlated. These figures also show the more subtle changes in BL vertical structure associated with the transition from a smaller percent of cumulus cloud cover to more widespread stratocumulus. As a diagnostic and parametric tool, Betts (1985, 1986) suggested that the BL could be characterized by $\beta = \partial p^*/\partial p$, the gradient of saturation pressure with pressure: $\beta = 0$ indicates a well-mixed layer and $\beta > 0$ a partially mixed one. Figures 5 and 7 support this approach. The cloudy BL is partially mixed with $\beta \approx 0.5$ for the whole layer $910 < p < 1010$ mb. Boers and Betts (1988) found a similar structure in a stratocumulus-capped layer. In contrast, the afternoon and low-cloud cover BL averages have a distinct two-layer structure, very similar to that found by Betts and Albrecht (1987) for trade wind cumulus BLs. For the subcloud layer ($960 < p < 1010$ mb), β has a smaller value, ≈0.3; while for the layer $900 < p < 960$ mb, $\beta \approx 1.0$, which a larger value characteristic of the more intermittent mixing found in cumulus layers.

However, although this confirms a correlation between cloud cover and vertical BL structure, it does not suggest a way of determining either within a parametric framework in a numerical model. Betts and Boers (1990) suggested from a study of a cloudiness transition in a marine BL that BL cloudiness might be linked to mean mixing-line slope. However, Albrecht (1991) found no evidence to support this from individual soundings from the R/V *Planet* during the Atlantic

Trade-Wind Experiment. However, the mean thermodynamic structures in Figs. 6 and 8 are consistent with Betts and Boers (1990).

Figure 9 shows a plot of θ_v against q for the low and high cloud-cover partition of the data. The solid upper curve corresponding to 80% cloud cover has a clearly steeper "mixing-line" slope within the BL than the lower 10% cloud cover curve (dotted). Both are curved profiles, however, because of radiative cooling in the moist BL (e.g., Betts 1982; Boers and Betts 1988). The corresponding sea surface temperature and pressures are the overlapping crosses. To get an estimate of the slope across the BL, we fitted regression lines to the data from 1010 mb to the points marked (860 mb for the low-cloud and 840 mb for the high cloud-cover composites). We fitted similar regression lines to the data from Fig. 4 for the morning and evening averages (not shown). The mixing-line slopes, defined as $\Gamma_M = (\partial\theta/\partial q)_M$ (i.e., in terms of θ rather than θ_v) were normalized by the corresponding slope of the wet adiabat, for which $\Gamma_W = (\partial\theta/\partial q)_W = -L\theta/C_pT$. Different selections of points in Fig. 9 will change the numerical results only slightly. Figure 10 reproduces Fig. 13 from Betts and Boers (1990) with these four ASTEX points added. The mean ASTEX data fit well with the points from earlier field programs, suggesting that mean cloud cover does have a transition close to the threshold $\Gamma_M/\Gamma_W \approx 0.5$. From a parametric viewpoint, however, this result is not entirely encouraging. The transition in cloud cover implied by Fig. 10 is rapid. The BL structure and cloud cover are closely coupled in the sense that the mean change of mean slope of Fig. 9 may well be caused by radiative processes, which are themselves linked in part to the cloud field. The next section shows that the BL structure of the ECMWF model up through the cloud layer is far from realistic.

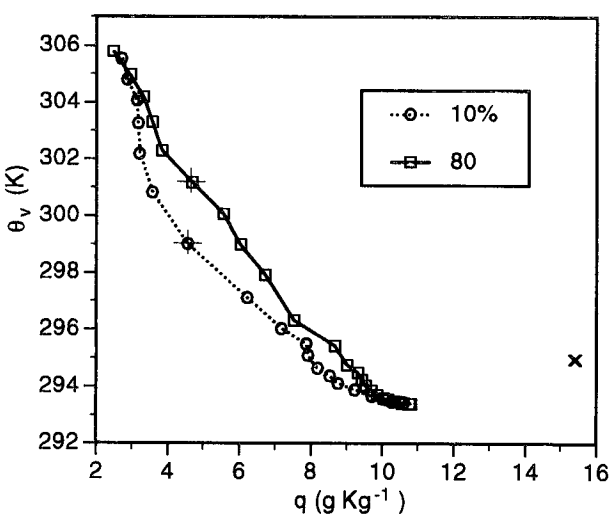

FIG. 9. Profile of θ_v against q for high and low cloud-cover partition.

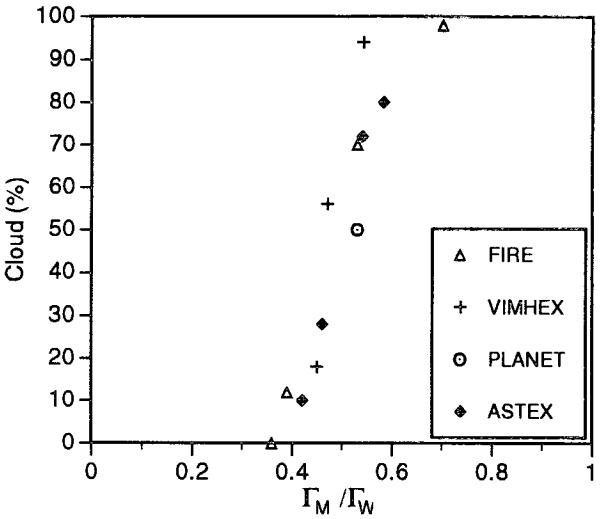

FIG. 10. Mean cloud cover against normalized mixing-line slope for different field experiments.

4. Comparison with ECMWF model

The ASTEX sonde data were assimilated into the ECMWF operational model both to compare the model BL structure with the observations and to use the model to analyze the vertical motion field over the ASTEX area. The analysis cycle times of the model are 0000, 0600, 1200, and 1800. From each analysis, 7-h short-range forecasts were run, and the model fields were archived every hour. In principle, this should give us the ability to explore the diurnal cycle using the model. In practice, from each analysis there is a spinup time of a few hours, so that there are discontinuities between an analysis and the 6-h forecast from the preceding analysis, particularly in the vertical motion field. We shall first compare the ECMWF-model structure at times corresponding closely to the morning and evening averages in Figs. 4–6 and then discuss the diurnal variation of the vertical motion field in the model.

a. ECMWF structure

Figure 11 shows the ECMWF model structure at the *Valdivia* at 0700 and 1900 averaged for the same period 8–14 June. These are the 1-h forecast structures from the 0600 and 1800 analyses. As noted by Bretherton et al. (1995), the ECMWF model does quite well in capturing the general temperature and moisture structure and inversion height (with 25-mb vertical resolution). The temperature range between 0700 and 1900 UT is less at low levels than in Fig. 6 and more at higher levels. (The ECMWF model in fact reaches a minimum temperature earlier in the night at low levels.) The morning average is uniformly moister than the evening one by about 0.3 g kg^{-1} (not shown). The biggest differences between the model and observations are in the

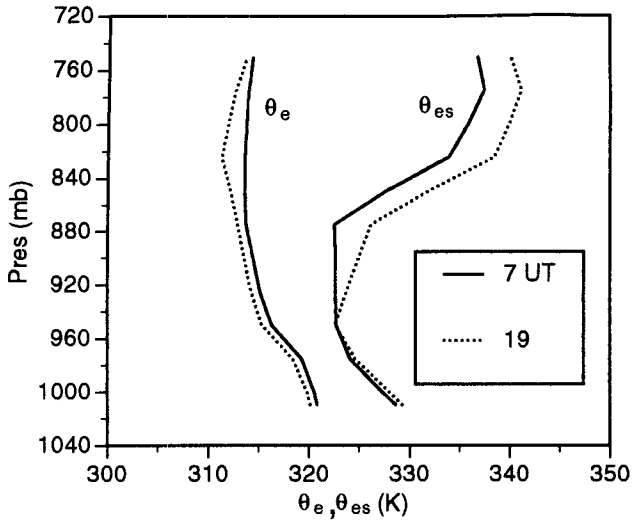

FIG. 11. As in Fig. 6 for ECMWF average profiles at 28°N, 24°W for 8–14 June.

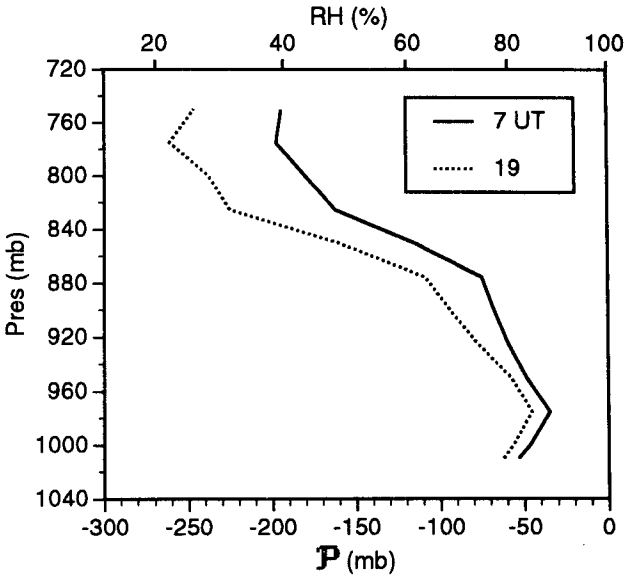

FIG. 12. As in Fig. 5 for ECMWF average profiles at 28°N, 24°W.

cloud layer from 875 to 950 mb. In comparison with Fig. 6, the ECMWF structure is much too warm and dry (and stable with respect to the moist adiabat), although the morning profile is less stable in the cloud layer than the evening one as in the data. This must mean that the upward convective transports in the ECMWF model, which would cool and moisten the cloud layer, are too weak. Figure 12 shows the corresponding ECMWF profile of $P = p^* - p$, showing the sharp increase in subsaturation above 975 mb in contrast to Fig. 5. Correspondingly, the model value of $\beta = \partial p^*/\partial p$ is too large. The cloud cover in the ECMWF model is determined by a diagnostic scheme. In ASTEX, low-cloud cover in the ECMWF model is determined primarily from the strength of the capping low-level inversion (Bretherton et al. 1995). The cloud cover diagnosed for the 0700 and 1900 profiles in Fig. 11 is 8% and 24%, respectively. The trend is incorrect, and the values are too low.

b. *ECMWF vertical motion field*

The ECMWF vertical motion field is less easy to analyze because of the model spinup every 6 h from each analysis time. Figure 13 shows the 7-day mean omega field in mb day^{-1} at 850 mb. The ordinate is UTC: we have also included the 7-day average for 7–13 June starting from the 1800 analysis, since these forecasts end at 0100. The mean value of 40 mb day^{-1} subsidence is reasonable (Betts and Ridgway 1988). However, the model omega field is very noisy, and the standard deviation between the 7 days is large ($\approx$45 mb day^{-1}), so it is not obvious that the variation has significance. The forecast sequences from each analysis appear to be disconnected. This seems to be due to model spinup. If we reject the model omega values for the first two forecast hours and connect (dotted) the remaining five segments, we get an apparent semidiurnal oscillation of omega, with a mean of 42 mb day^{-1} and almost as large an amplitude. Without an independent direct budget analysis of the ASTEX sonde data, we cannot however assess whether this oscillation of the omega field in the ECMWF model is real or is produced by the model analysis scheme. It is out of phase with the observed surface semidiurnal pressure oscil-

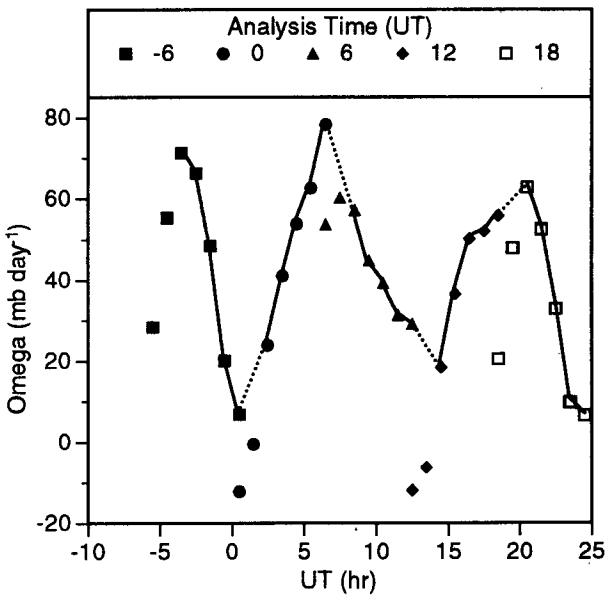

FIG. 13. Time variation of mean 850-mb omega in ECMWF model at 28°N, 24°W.

lation at the *Valdivia,* which has an amplitude of 1.5 mb for this week. This needs further study. In retrospect, it would have been preferable to do 24- or 30-h forecasts with the model and study the diurnal variation of omega in these.

c. *ECMWF mean advection*

We believe that the observed BL profiles may be useful for modeling studies. Since we have no direct estimates of the large-scale advection terms or the geostrophic wind, we are including, as Table A3, the 7-day low-level mean profiles at 28°N, 24°W from the ECMWF analysis for the wind components u and v, the geostropic wind u_g and v_g, the horizontal advection of temperature and moisture T_{adv} and q_{adv}, and the vertical advection ω. Within the BL (surface to 900 mb) T_{adv}, q_{adv} have mean values of approximately -1.43 K day^{-1} and -0.44 g kg^{-1} day^{-1}, roughly consistent with one day's low-level advection over warmer water. In view of the large variations seen in the model short-term forecasts of the omega field, these 7-day means (from the model analysis) should be used with caution.

5. Conclusions

We have analyzed a week of BL data at the R/V *Valdivia* during the period it was located at 28°N, 24°W for ASTEX. The ceilometer data shows a large diurnal variation of BL cloudiness. Despite some apparent problems with solar heating of the radiosonde sensors during the day, we can see a clear change in mean BL structure between predawn and early evening, associated with the change in cloudiness. At night, the BL is radiatively destabilized; it becomes close to saturation just below the inversion as layer clouds develop, although the BL as a whole never becomes well mixed. During the daytime, solar heating warms and stabilizes the BL; the layer cloud thins, and the late afternoon BL structure shows a more well-mixed subcloud layer, below a less well mixed cloud layer, more characteristic of the trade wind cumulus layer seen in other studies. Partitioning the data by ceilometer cloud fraction shows a similar picture with a slightly sharper separation. Although we are able to show the link between BL cloudiness and thermodynamic structure, this alone does not give a satisfactory parametric model for the transition, which involves the coupling between cloud-scale transports and the radiation field. The mean profiles, however, are consistent with the suggestion of Betts and Boers (1990) that there is a transition in cloudiness at a normalized BL mixing-line slope $\Gamma_M/\Gamma_W \approx 0.5$.

We show for comparison the sunrise and sunset BL structure in the ECMWF model for the same time period, which determines cloud cover largely from a diagnostic scheme coupled to inversion strength. Although the subcloud layer and inversion height in the model are a reasonable representation of the data, the "cloud" layer in the model is too warm, stable, and dry in comparison with the observations, as noted also in Bretherton et al. (1995). The ECMWF-model omega field shows spinup from each analysis and an apparent semidiurnal oscillation of large amplitude, for which we have no confirmatory evidence.

The observed profiles shown in Figs. 4–8 could be used as test datasets to develop BL models and parametric schemes for fractional cloudiness and the diurnal variation of the oceanic boundary layer. The mean soundings are tabulated in the appendix, as Tables A1 and A2, followed in Table A3 by 7-day mean low-level profiles of the geostrophic wind, omega field, and horizontal advection derived from the ECMWF analysis.

Acknowledgments. A. Betts was supported by NASA under Contract NAS5-31738 and the NSF under Grant ATM9001960. C. Bretherton was supported by ONR Grant N00014-90-J-1136. Much of this work was completed while they were visiting scientists at ECMWF. Ceilometer and radiosonde data for the R/V *Valdivia* were provided by Dr. G. Kruspe of the Max-Planck-Institute, Hamburg, Germany, and processed by W. Syrett at The Pennsylvania State University.

APPENDIX

Mean Profiles from Soundings and from ECMWF Analyses

TABLE A1.

Morning average (0630 UTC)					Evening average (1830 UTC)				
p (mb)	T (K)	Q (g Kg^{-1})	U (m s^{-1})	V (m s^{-1})	p (mb)	T (K)	Q (g Kg^{-1})	U (m s^{-1})	V (m s^{-1})
150.0	−65.3	0.0	32.9	8.7	150.0	−64.9	0.0	31.5	12.3
200.0	−57.8	0.0	33.2	8.2	200.0	−57.6	0.0	28.8	12.8
250.0	−46.7	0.1	28.6	6.1	250.0	−46.8	0.1	25.9	9.9
300.0	−36.9	0.2	22.7	4.1	300.0	−36.6	0.2	21.3	6.6
350.0	−28.6	0.3	17.7	3.5	350.0	−28.0	0.4	16.3	5.3
400.0	−21.5	0.5	12.9	2.3	400.0	−20.8	0.5	12.0	2.5
450.0	−15.7	0.7	11.3	1.6	450.0	−15.3	0.9	9.5	1.6
500.0	−10.5	1.0	9.2	0.6	500.0	−10.0	1.1	8.8	−0.2
550.0	−5.4	1.4	7.5	−0.4	550.0	−5.0	1.5	7.2	−1.7
600.0	−0.7	1.9	7.0	−1.7	600.0	−0.2	2.4	5.8	−2.7
650.0	3.8	2.2	5.2	−2.8	650.0	4.3	2.5	4.6	−3.2
700.0	7.37	2.33	3.0	−3.5	700.0	8.10	2.16	2.7	−2.9
710.0	7.95	2.35	2.5	−3.4	710.0	8.75	2.09	2.4	−2.9
720.0	8.60	2.42	1.8	−3.3	720.0	9.37	2.30	1.9	−2.8
730.0	9.26	2.52	1.3	−3.4	730.0	10.00	2.41	1.6	−2.9
740.0	9.84	2.61	0.7	−3.3	740.0	10.67	2.46	1.2	−2.9
750.0	10.40	2.49	0.1	−3.4	750.0	11.35	2.28	0.8	−3.0
760.0	10.93	2.37	−0.4	−3.6	760.0	11.82	2.28	0.4	−3.2
770.0	11.47	2.55	−1.0	−3.9	770.0	12.19	2.34	0.0	−3.2
780.0	11.93	2.61	−1.5	−4.1	780.0	12.56	2.44	−0.6	−3.3
790.0	12.27	2.64	−1.9	−4.3	790.0	12.89	2.43	−1.0	−3.5
800.0	12.62	2.78	−2.3	−4.5	800.0	13.13	2.82	−1.4	−3.5
810.0	12.93	2.80	−2.7	−4.5	810.0	13.39	2.94	−1.7	−3.6
820.0	13.19	2.70	−3.2	−4.5	820.0	13.50	3.55	−2.3	−3.6
830.0	13.11	3.04	−3.8	−4.4	830.0	13.85	3.68	−2.4	−3.7
840.0	12.45	4.06	−4.2	−4.4	840.0	14.05	3.46	−3.0	−3.9
850.0	11.75	5.25	−4.5	−4.6	850.0	13.64	3.85	−3.5	−4.0
860.0	11.32	6.13	−4.8	−4.8	860.0	12.91	4.71	−4.0	−4.2
870.0	11.23	6.92	−5.0	−4.8	870.0	11.92	6.17	−4.4	−4.4
880.0	10.59	7.48	−5.0	−5.0	880.0	11.57	7.05	−4.7	−4.5
890.0	10.60	8.24	−5.1	−5.2	890.0	11.62	8.07	−5.1	−4.7
900.0	10.97	8.55	−5.1	−5.3	900.0	11.91	8.28	−5.4	−4.7
910.0	11.66	8.87	−5.3	−5.5	910.0	12.38	8.41	−5.6	−4.8
920.0	12.36	9.01	−5.3	−5.6	920.0	12.93	8.68	−5.7	−4.8
930.0	13.01	9.18	−5.5	−5.5	930.0	13.55	8.96	−5.8	−4.9
940.0	13.68	9.40	−5.6	−5.6	940.0	14.15	9.37	−6.0	−5.0
950.0	14.36	9.68	−5.7	−5.6	950.0	14.73	9.81	−5.9	−5.1
960.0	15.06	9.97	−5.8	−5.5	960.0	15.48	10.08	−5.8	−5.4
970.0	15.86	10.12	−5.8	−5.5	970.0	16.28	10.08	−5.8	−5.6
980.0	16.64	10.24	−5.8	−5.4	980.0	17.10	10.26	−5.5	−5.1
990.0	17.37	10.50	−5.8	−5.0	990.0	17.90	10.35	−5.8	−5.1
1000.0	18.14	10.74	−5.4	−4.7	1000.0	18.74	10.48	−5.7	−4.9
1010.0	18.97	10.76	−5.2	−4.2	1010.0	19.53	10.48	−5.6	−4.7
1021.3	19.85	11.03	−5.7	−4.0	1021.5	20.34	10.94	−5.1	−4.5
Sea surface data					Sea surface data				
1021.3	20.82	15.34			1021.5	20.99	15.50		

TABLE A2.

Low-cloud average (10%)					High-cloud average (80%)				
p (mb)	T (K)	Q (g Kg^{-1})	U (m s^{-1})	V (m s^{-1})	p (mb)	T (K)	Q (g Kg^{-1})	U (m s^{-1})	V (m s^{-1})
150.0	−65.4	0.0	29.7	11.6	150.0	−64.7	0.0	35.7	8.0
200.0	−57.7	0.0	30.1	12.7	200.0	−57.7	0.0	34.5	6.6
250.0	−47.0	0.1	26.8	10.5	250.0	−46.7	0.1	30.2	5.0
300.0	−36.9	0.2	22.8	8.2	300.0	−36.9	0.2	23.1	1.4
350.0	−28.5	0.4	18.5	7.0	350.0	−28.5	0.3	16.0	0.8
400.0	−21.4	0.5	14.1	4.0	400.0	−21.2	0.4	11.1	−0.1
450.0	−15.9	0.8	10.6	2.4	450.0	−15.2	0.6	9.5	−0.6
500.0	−10.5	1.1	8.9	1.3	500.0	−10.2	1.0	8.3	−2.0
550.0	−5.3	1.1	6.7	0.1	550.0	−5.3	1.5	6.8	−2.9
600.0	−0.7	2.2	6.2	−0.7	600.0	−0.5	1.8	6.0	−3.9
650.0	3.8	2.5	4.0	−1.4	650.0	3.8	2.3	4.8	−4.5
700.0	7.83	2.36	2.2	−1.8	700.0	7.37	2.07	3.0	−4.6
710.0	8.49	2.29	2.0	−1.9	710.0	7.89	2.10	2.4	−4.5
720.0	9.11	2.43	1.7	−2.0	720.0	8.50	2.30	1.6	−4.3
730.0	9.80	2.49	1.3	−2.1	730.0	9.12	2.52	1.1	−4.3
740.0	10.44	2.49	1.0	−2.2	740.0	9.81	2.61	0.6	−4.2
750.0	11.04	2.53	0.6	−2.3	750.0	10.47	2.46	0.1	−4.3
760.0	11.57	2.30	0.3	−2.5	760.0	10.96	2.40	−0.4	−4.5
770.0	11.91	2.35	−0.2	−2.6	770.0	11.48	2.66	−0.8	−4.7
780.0	12.34	2.42	−0.7	−2.8	780.0	11.95	2.67	−1.2	−4.8
790.0	12.71	2.53	−1.1	−3.0	790.0	12.29	2.46	−1.7	−4.9
800.0	13.03	2.71	−1.5	−3.2	800.0	12.45	2.94	−2.2	−4.9
810.0	13.32	2.86	−1.9	−3.3	810.0	12.67	3.30	−2.7	−4.9
820.0	13.59	3.13	−2.5	−3.5	820.0	12.80	3.56	−3.2	−4.8
830.0	13.82	3.17	−2.9	−3.6	830.0	12.79	3.82	−3.7	−4.7
840.0	13.78	3.21	−3.4	−3.7	840.0	12.57	4.67	−4.2	−4.7
850.0	13.38	3.57	−3.9	−3.8	850.0	12.32	5.54	−4.5	−4.8
860.0	12.46	4.54	−4.4	−4.0	860.0	12.17	6.02	−4.8	−5.0
870.0	11.29	6.21	−4.8	−4.1	870.0	11.97	6.71	−4.9	−5.3
880.0	11.01	7.17	−5.1	−4.2	880.0	11.22	7.52	−4.8	−5.5
890.0	11.28	7.87	−5.4	−4.4	890.0	11.09	8.67	−5.0	−5.7
900.0	11.79	7.92	−5.7	−4.5	900.0	11.29	9.01	−5.0	−5.8
910.0	12.22	8.19	−6.0	−4.5	910.0	11.89	9.31	−5.1	−6.0
920.0	12.80	8.53	−6.1	−4.6	920.0	12.52	9.41	−5.0	−6.1
930.0	13.38	8.76	−6.2	−4.6	930.0	13.18	9.52	−5.2	−6.1
940.0	13.96	9.22	−6.3	−4.7	940.0	13.86	9.68	−5.3	−6.2
950.0	14.53	9.70	−6.3	−4.7	950.0	14.56	9.85	−5.2	−6.1
960.0	15.21	10.07	−6.3	−4.8	960.0	15.26	10.03	−5.2	−5.9
970.0	15.95	10.27	−6.2	−4.9	970.0	16.06	10.15	−5.3	−5.8
980.0	16.76	10.48	−5.9	−4.6	980.0	16.82	10.35	−5.3	−5.7
990.0	17.57	10.51	−6.3	−4.9	990.0	17.56	10.54	−5.3	−5.3
1000.0	18.41	10.61	−6.3	−4.7	1000.0	18.33	10.76	−5.0	−5.0
1010.0	19.23	10.60	−6.2	−4.5	1010.0	19.15	10.79	−4.8	−4.5
1022.2	20.11	10.86	−5.6	−4.0	1021.3	19.97	11.11	−5.0	−4.4
Sea surface data					Sea surface data				
1022.2	20.91	15.42			1021.3	20.85	15.37		

TABLE A3. Seven-day mean ECMWF profiles.

Pressure (mb)	U (m s^{-1})	U_g (m s^{-1})	V (m s^{-1})	V_g (m s^{-1})	T_{adv} (K day^{-1})	Q_{adv} (K day^{-1})	Omega (mb day^{-1})
750	−1.11	−0.95	−4.23	−4.29	−2.70	−0.22	45.2
775	−2.51	−1.99	−4.10	−4.17	−2.75	0.07	40.8
800	−3.47	−2.98	−4.21	−4.03	−2.59	0.30	38.0
825	−4.29	−3.71	−4.39	−4.03	−2.45	0.58	35.8
850	−4.82	−4.33	−4.71	−3.94	−1.44	0.15	32.9
875	−5.31	−4.90	−5.04	−4.31	−0.68	−0.20	32.0
900	−5.68	−5.36	−5.39	−4.49	−1.00	−0.23	30.4
925	−5.99	−5.71	−5.70	−4.60	−1.24	−0.20	27.8
950	−6.23	−6.07	−5.96	−4.57	−1.37	−0.18	23.3
975	−5.98	−6.42	−5.95	−4.55	−1.56	−0.68	17.4
1000	−5.74	−6.78	−5.83	−4.51	−1.63	−0.65	13.5
1010	−5.58	−6.86	−5.67	−4.44	−1.83	−0.69	11.1

REFERENCES

Albrecht, B. A., 1991: Fractional cloudiness and cloud-top entrainment instability. *J. Atmos. Sci.*, **48,** 1519–1525.

——, C. S. Bretherton, and D. Johnson, 1995a: The Atlantic Stratocumulus Transition Experiment (ASTEX). *Bull. Amer. Meteor. Soc.*, **76,** 889–904.

——, M. P. Jensen, and W. J. Syrett, 1995b: Marine boundary structure and fractional cloudiness. *J. Geophys. Res.*, in press.

Betts, A. K., 1982: Saturation point analysis of moist convective overturning. *J. Atmos. Sci.*, **39,** 1484–1505.

——, 1985: Mixing line analysis of clouds and cloudy boundary layers. *J. Atmos. Sci.*, **42,** 2751–2763.

——, 1986: A new convective adjustment scheme. Part I: Observational and theoretical basis. *Quart. J. Roy. Meteor. Soc.*, **112,** 677–692.

——, 1990: Diurnal variation of California coastal stratocumulus from two days of boundary layer soundings. *Tellus*, **42A,** 302–304.

——, and B. A. Albrecht, 1987: Conserved variable analysis of boundary layer thermodynamic structure over the tropical oceans. *J. Atmos. Sci.*, **44,** 83–99.

——, and W. Ridgway, 1988: Coupling of the radiative, convective, and surface fluxes over the equatorial Pacific. *J. Atmos. Sci.*, **45,** 522–536.

——, and R. Boers, 1990: A cloudiness transition in a marine boundary layer. *J. Atmos. Sci.*, **47,** 1480–1497.

Boers, R., and A. K. Betts, 1988: Saturation point structure of marine stratocumulus clouds. *J. Atmos. Sci.*, **45,** 1157–1175.

Bretherton, C. S., E. Klinker, A. K. Betts, and J. A. Coakley, 1995: Comparison of ceilometer, satellite, and synoptic measurements of boundary layer cloudiness and the ECMWF diagnostic cloud parameterization scheme during ASTEX. *J. Atmos. Sci.*, **52,** 2736–2751.

Cole, H., 1993: The TOGA-COARE ISS radiosonde temperature and humidity sensor errors. NCAR Tech. Rep. SSSF, 26 pp.

Kloessel, K. A., and B. A. Albrecht, 1989: Low-level inversions over the tropical Pacific: Thermodynamic structure of the boundary layer and the above-inversion moisture structure. *Mon. Wea. Rev.*, **117,** 87–103.